Shot record depth migration of georadar

Robert J. Ferguson, Adam Pidlisecky, and Colin Rowell

ABSTRACT

We modify common shot record migration from seismic imaging into a single trace prestack depth migration (PSDM) specifically for georadar. Implemented using a combination of Linux, Pearl, and Octave programming languages, our georadar PSDM runs in parallel on the CREWES cluster Gilgamesh. This PSDM migrates the radar data from topography, and when compared to conventional migration derived from normal-incidence topography correction followed by zero-offset migration, we find that our PSDM returns significantly improved migrated images. As part of pre-image processing, we find that nonstationary deconvolution implemented in the Gabor domain significantly enhances the sharpness of reflection and diffraction events, and it significantly enhances reflection and diffraction arrivals at later times when compared to conventional spiking deconvolution.

INTRODUCTION

Similar to electromagnetic propagation in ice, the low dielectric permittivity of basalt causes strong electromagnetic reflections from interfaces (Finlay et al., 2008), and because the low conductivity of basalt allows a great depth of penetration (Jol, 2009; Sen et al., 2003), georadar is well suited to image structures within basalt.

At Craters of the Moon, Idaho, USA, a large basalt flood contains a plumbing system of volcanic conduits. Some conduits are so well known that they are open to tourists, while others are unknown and unexplored (Rowel et al., 2010). To understand the origins and extent of the basalt flow, there is great interest in complete characterization of this conduit system, and an initial interpretation is provided in a companion paper by Rowel et al. (2010) in this volume. The target conduits are metres in height and circumference, so georadar soundings must be acquired with sub-decimetre bin spacings. Such small targets require processing and imaging far beyond what is the common practice Slob et al. (2010). So in this paper, we adapt our advanced seismic processing, imaging, and inversion for 2D georadar imaging.

We use a single line as a demonstration of our processing and imaging approach, and we begin this work with a brief summary of the acquisition parameters for this line. Though our acquisition approach allowed us to acquire a large amount of data in a short time, it did result in irregular spacing of georadar soundings. As a remedy we develop a sequence of data preparation steps where the survey geometry is simplified, and then we interpolate the elevation and georadar data onto a regular grid. Spiking deconvolution (Robinson and Treitel, 1980) and Gabor deconvolution (Margrave et al., 2005) are compared in a processing section, and then topographic correction followed by zero offset migration is compared to our new PSDM designed for georadar. In this latter discussion, we provide an outline of our parallel implementation of georadar PSDM.

GEORADAR ACQUISITION

Georadar data were acquired for 21 lines at the Craters of the Moon site for use in characterizing the subsurface network of volcanic flow tubes (Rowel et al., 2010). Here, we will concentrate on the processing and imaging aspects of this work using line 23 from that data volume. Table 1 provides a summary of acquisition parameters for this line, as well as some preliminary processing parameters deduced from data analysis - specifically $c = 14{,}000$ cm$/\mu$s for the speed of light in basalt, and f_{min} = 20 MHz and f_{max} = 200 MHz for the max and min temporal frequencies of interest. The nominal trace spacing $\Delta x = 10$ cm is intended to capture unaliased all radar reflections (Grasmueck et al., 2005), however, the basalt surface was rugged and $0 \leq \Delta x \leq 10$'s of centimetres resulted in a median $\Delta x_{med} \sim 14$ cm. Table 1 also reports values for depth (Δz, and z_{max}), and these are the interval for depth imaging and maximum image depth respectively. These values will be used in depth imaging later.

Line #	23
f_{cent}	100 MHz
f_{min}	20 MHz
f_{max}	200 MHz
c	14,000 cm / μ s
x_{offset}	100 cm
Δx	10 cm
Δz	5 cm
z_{max}	1200 cm

Table 1. Acquisition parameters (Rowel et al., 2010).

Note, during acquisition, the acquisition unit is set to acquire traces continuously at a fixed acquisition time interval. This means that when acquisition is halted, redundant traces are acquired for the corresponding spatial location. As the next section describes, these redundant traces are deleted, however, in future, they should be accommodated as extra data for imaging.

DATA PREPARATION

Data preparation prior to processing and imaging consists of (see Table 2): 1) Survey rotation. 2) Elevation interpolation. 3) Delete top pad. 4) Trace interpolation. Survey rotation (1) was done to simplify the survey for later processing steps. Survey data were read in from the headers, the survey origin was shifted to $(0, 0)$, and a rotation operator was determined to minimize variation in the Northerly direction according to

Process	Parameters
Rotate survey	Linear fit
Interpolate elevations	Linear interpolation ($\Delta x \sim 14$ cm)
Align $t = 0$ for traces	Delete top pad
Interpolate traces	Linear interpolation ($\Delta x \sim 14$ cm)

Table 2. Data preparation parameters.

$$\begin{bmatrix} X \\ Y \end{bmatrix} = \begin{bmatrix} \cos\theta & -sin\theta \\ \sin\theta & \cos\theta \end{bmatrix} \begin{bmatrix} x \\ y \end{bmatrix}, \tag{1}$$

where (X, Y) and (x, y) are the rotated and original coordinates respectively, and θ is the rotation angle. A linear polynomial fit to the survey data is used to determine θ, where $\tan\theta$ is taken from the first order term of the polynomial.

The input survey and the rotated survey are depicted in Figure 1a, where the survey, the

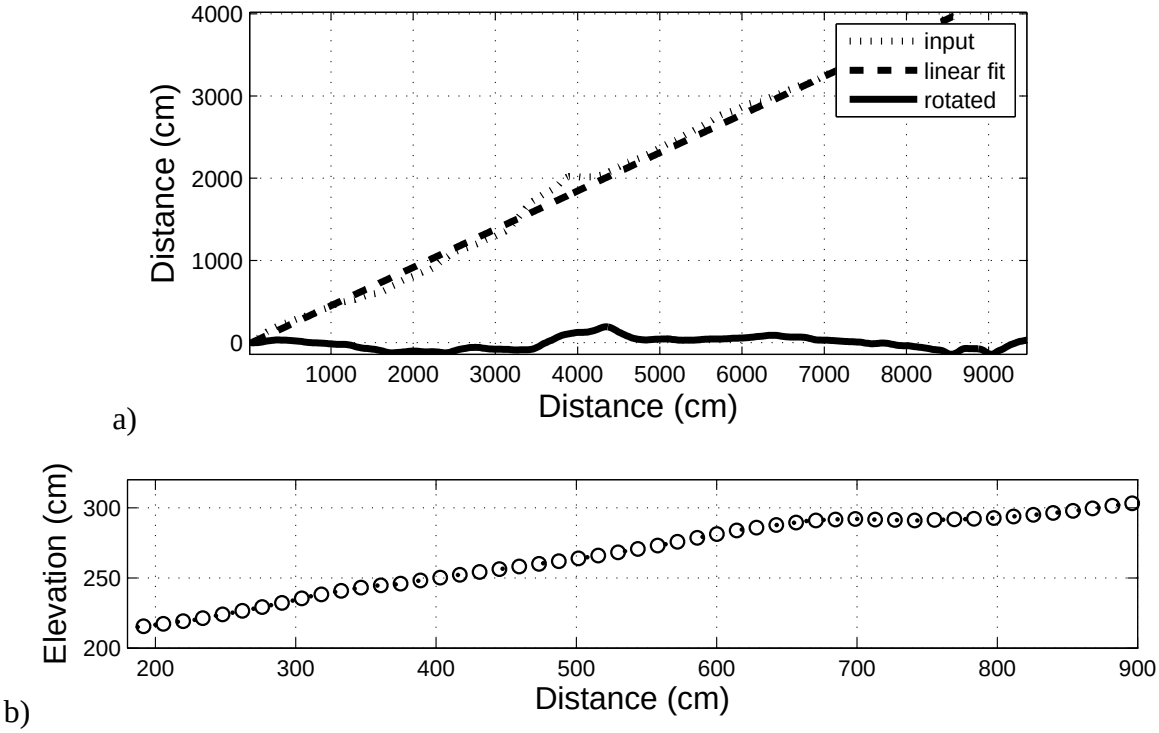

FIG. 1. Survey parameters. a) The survey is rotated to minimize variation along the ordinal. b) Elevations are interpolated onto a regular grid.

linear fit, and the rotated survey are given by dotted, dashed, and solid lines respectively. Spatial variation of the rotated survey about the zero line is then ignored, and the horizontal component is differentiated. The differentiated result is then analyzed for zero values to indicate redundant traces. Redundant traces are then eliminated. Because later imaging proceedures are based on spatial FFTS, data must be evenly sampled. The data acquired here, however, are irregularly sampled about a goal interval of 10 cm (Table 1). A value of $\Delta x = 14\,\mathrm{cm}$, then, is computed from the median of the differentiated horizontal distance.

Indicated by dots in Figure 1b, the original irregular elevation survey is interpolated from the true survey locations onto a regular grid $(\Delta x = 14\,\mathrm{c})$ indicated by circles on this Figure. This range of data (200 - 900 cm distance) represents the most irregular section of the entire survey. The next interpolation step (3), is to map the data onto the regular grid, and this is done using linear interpolation as well. A close up on the most irregular range (200 - 900 cm distance) indicates a satisfactory result in that reflection events appear to be coherent and well sampled. This is a qualitative result, of course, and no attempt is made here to analyze the effects of spatial aliasing.

DATA PROCESSING

Data processing consists of two approaches to georadar deconvolution. The first, as a benchmark, is conventional spiking deconvolution (Robinson and Treitel, 1980) applied to whiten the frequency spectrum of the input data. Then, Gabor deconvolution (Margrave

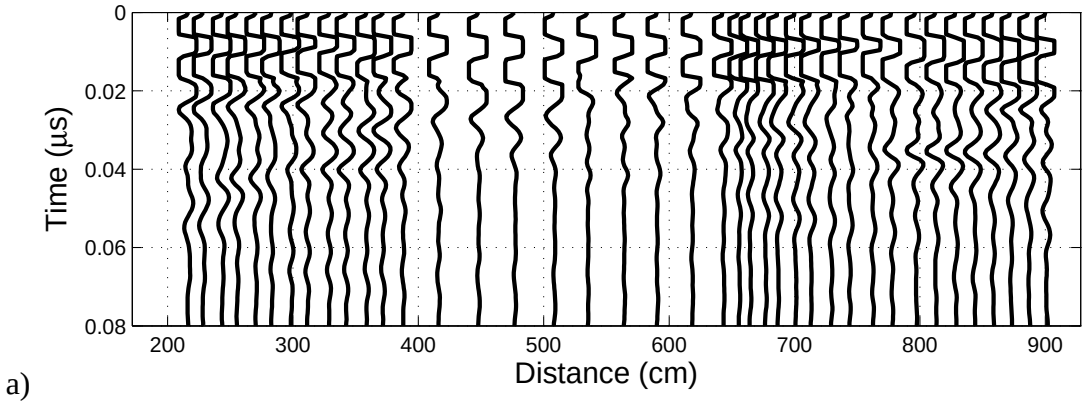

a)

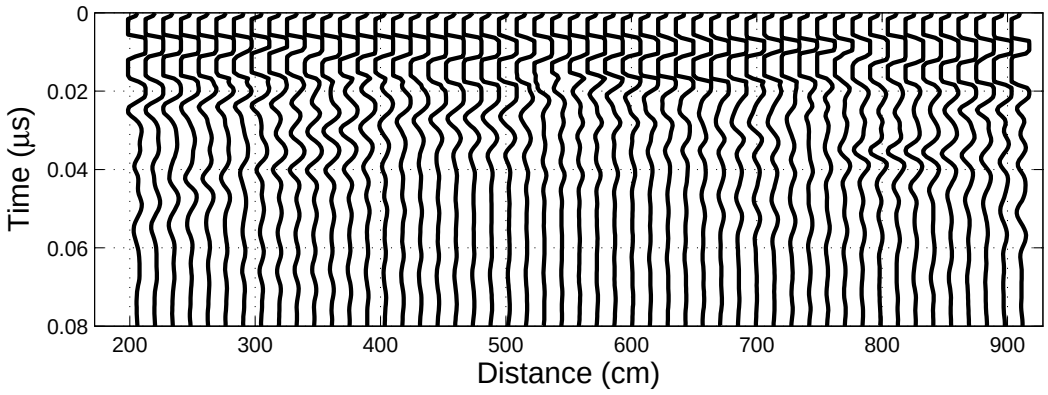

b)

FIG. 2. Data regularization. a) Data from the original survey have irregular trace spacing. b) Data from (a) interpolated onto a regular grid.

et al., 2005) is applied in an iterative process where the numerous input parameters are varied. Iteration stops when the best result relative to the spiking deconvolution benchmark is achieved.

Spiking deconvolution

From the CREWES Matlab Toolbox, `deconf` was selected, and through experimentation, a parametrization of a 17 point boxcar filter applied to the input spectrum and a stabilization factor of 10^{-4} (Table 3) produces the most satisfactory, zero-phase result. For comparison, the raw data and spectrum are shown in Figures 3a and b respectively, and the deconvolved output is given in Figures 4a and b. Note, the usable frequency range is between about 20 Hz and 150 Hz, though in imaging (next section) we use an optimistic 200 MHz as the maximum. Spiking deconvolution flattens the spectrum as desired (Figure 4b), and reflection events are generally more coherent (Figure 4a); In particular, reflections and diffractions above ~ 0.125 μs are more distinct indicating significant removal of *ringing*.

Parameter	Value
Design trace	Design on trace
# points in f boxcar	17
Stabilization factor	0.0001
Output phase	Zero

Table 3. Spiking deconvolution (Robinson and Treitel, 1980) parameters.

Gabor deconvolution

The georadar source waveform is known to be even more nonstationary that the seismic waveform (L. R. Bentley, personal communication), so we employ the nonstationary deconvolution of Margrave et al. (2005). Implemented in the Gabor domain, `gabordeconb` from the CREWES Matlab Toolbox computes and applies a time-variant deconvolution operator to the input data (Margrave et al., 2005) where the time-variant operator approximates the true correction for a dispersive source wavefield. Input parameters to `gabordeconb` are fairly numerous, so an iterative procedure was employed to converge to suitable values as is summarized in Table 4. The resultant data and spectrum are given in Figures 5a and b. In comparison with spiking deconvolution (Figures 4)a and b, Gabor deconvolution does not seem to broaden the frequency range beyond what is achievable with spiking deconvolution, however, individual events are certainly sharper - especially above 0.05 μs, and it has brought out reflection and diffraction energy below 0.125 μs. The improvement below 0.125 μs has prompted us to return to this site to acquire longer records as there is clear reflection energy down to the end of the recordings.

Parameter	Value
Gaussinan window width	0.12 μs
Window increment	0.0024 μs
Width of t smoother	0.016 μs
Width of f smoother	110 MHz
Smoothing	Hyperbolic
Order of Burg spec.	10
Stability factor	0
Phase of output	0
Synthesis window	Unity

Table 4. Gabor deconvolution (Margrave et al., 2005) parameters.

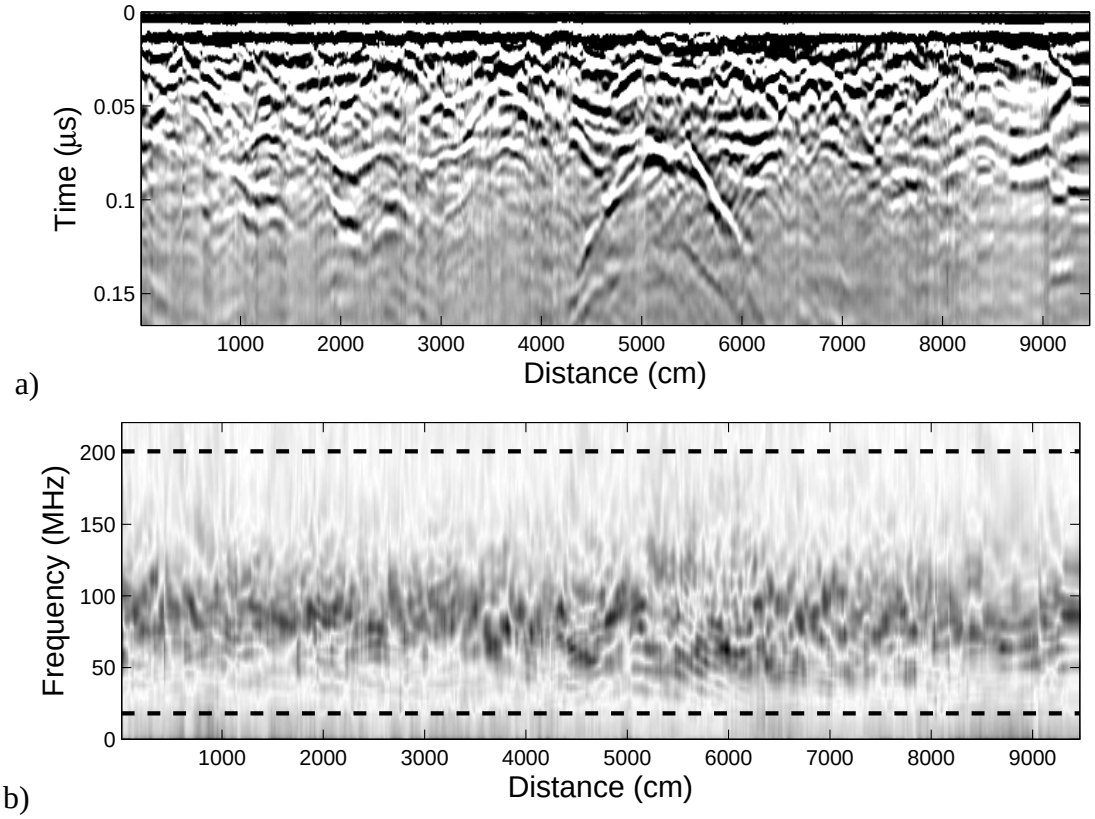

FIG. 3. The raw data. a) The regularized raw data. b) The spectrum of the raw data. Note the dominant frequency at 100 MHz.

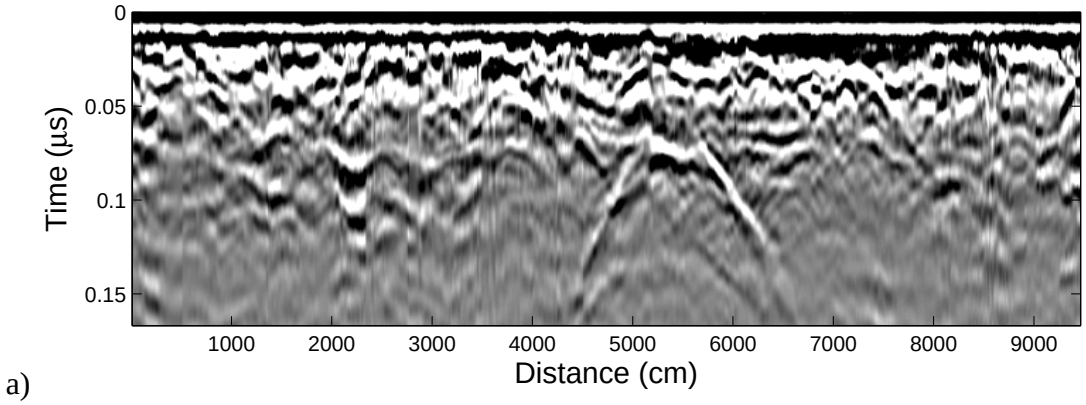

a)

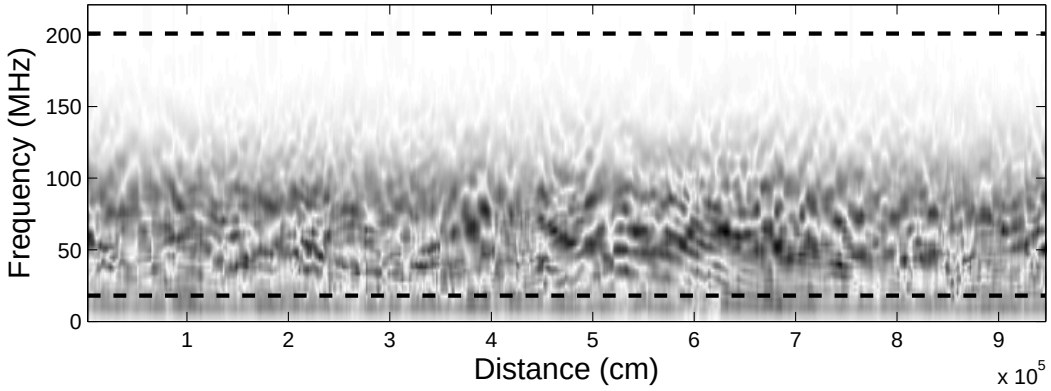

b)

FIG. 4. Spiking deconvolution Robinson and Treitel (1980) of the raw data. a) The deconvolved output. b) The spectrum of the deconvolved output. Spiking deconvolution has recovered some low-frequency, with minimal gain of higher frequency.

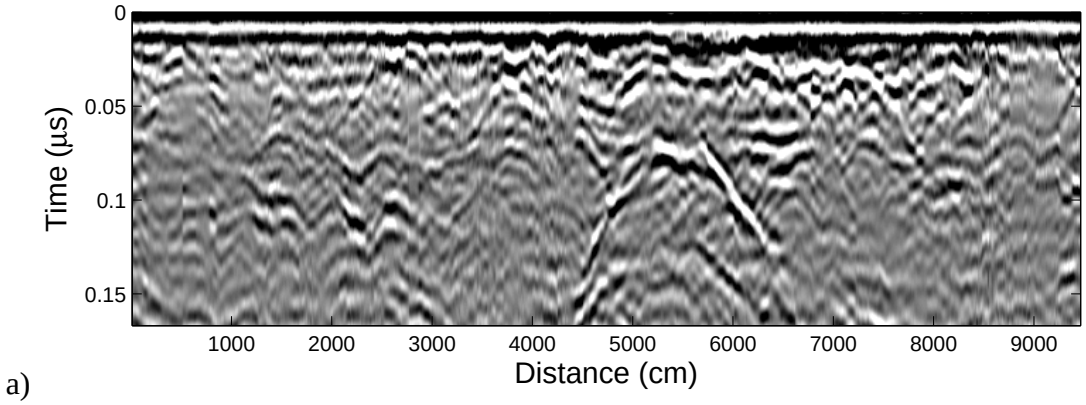

a)

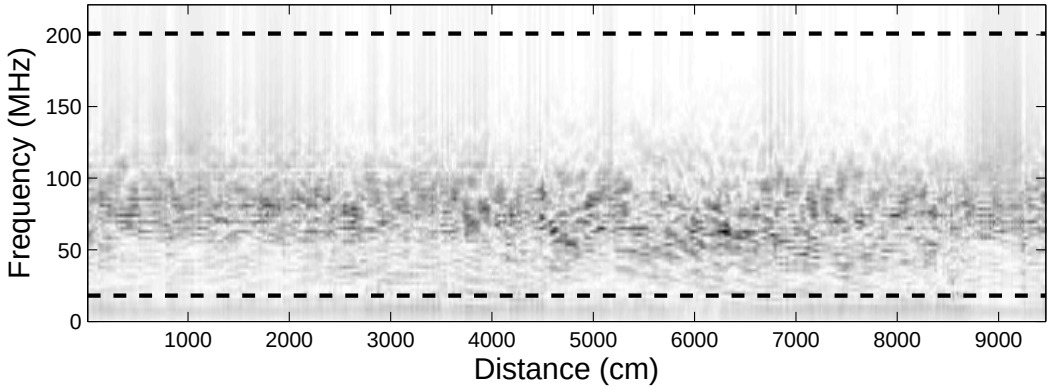

b)

FIG. 5. Gabor deconvolution Margrave et al. (2005) of the raw data. a) The deconvolved output. b) The spectrum of the deconvolved output. Gabor deconvolution has recovered low-frequency, and events appear sharper than spiking deconvolution (Figure 4).

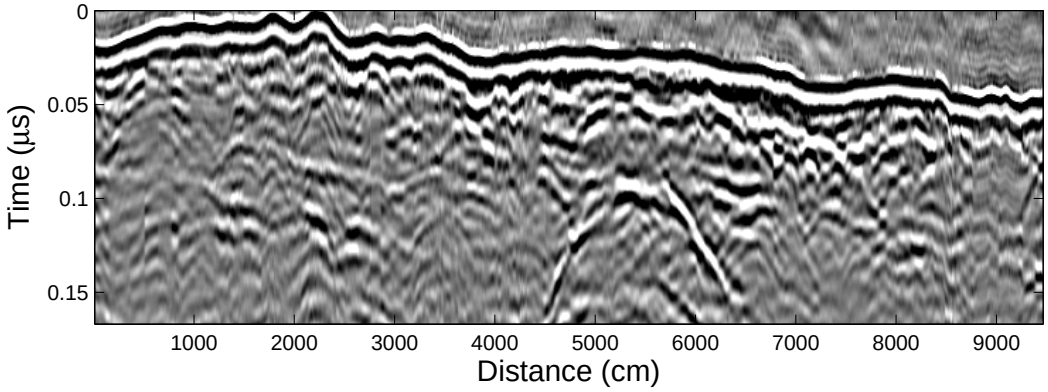

FIG. 6. Input data for zero-offset migration. These data have Gabor deconvolution (Margrave et al., 2005) and statics applied.

Zero offset migration

Zero-offset migration (ZOM) is used here as a first look at the subsurface structure in depth; In conventional georadar imaging, ZOM is usually the stopping point of most georadar imaging efforts. Bistatic georadar, of course, is not a zero-offset experiment (here *offset* = 100 cm), and we find that significant improvement comes as a result of using prestack depth migration (PSDM) instead (next section).

Nearsurface topography plays a significant role in the structure of reflection and diffraction events, so we correct the data prior to ZOM. Correction is done by computing first the $t \Rightarrow f$ spectrum $\tilde{\psi}$ of the data according to

$$\tilde{\psi}_0 (x, \omega) = \frac{1}{2\,\pi} \int \psi_0 (x, t)\, e^{-i\,\omega\,t} dt, \tag{2}$$

where ψ_0 is a trace recorded at surface position x, t is recording time, and $\omega = 2\,\pi\,f$ (for brevity, the $\pm\infty$ limits are not shown). Using the elevation survey $z\,(x)$, spectrum $\tilde{\psi}$ is corrected for traveltime according to

$$\tilde{\psi}_{z(x)} (x, \omega) = \tilde{\psi}_0 (x, \omega)\, e^{i\,\mathrm{sign}(\omega)\,2\,\omega\,\Delta z(x)/c}, \tag{3}$$

where "sign" is the *signum* function,

$$\Delta z\,(x) = z\,(x) - \mathrm{MAX}\,\{z\,(x)\}\,, \tag{4}$$

and

$$\psi_{z(x)} (x, t) = \int \tilde{\psi}_{z(x)} (x, \omega)\, e^{i\,\omega\,t} d\omega. \tag{5}$$

Output data ψ_z appears now as if it were acquired along a datum below which is basalt with velocity $c = 14,000$ cm / μs (Table 1). Figure 6 shows the result of this correction. Rather than horizontal first arrivals, the first arrival aligns at t=0 only a distances x that correspond to the maximum elevation MAX $\{z\,(x)\}$ in equation 4.

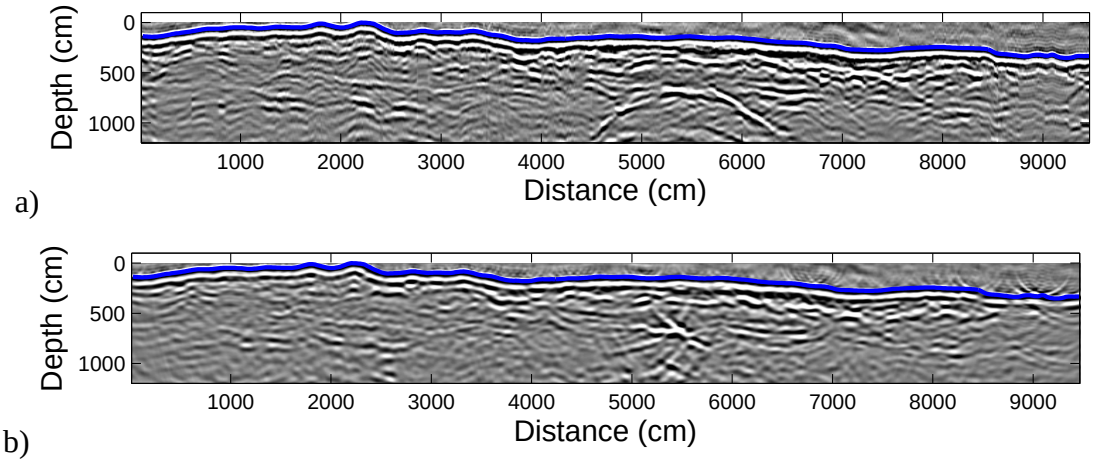

FIG. 7. Zero offset migration. a) The input data (Figure 6) are stretched to depth for comparison. b) Zero-offset migration output. The elevation profile is overlain as a solid line.

ZOM is then applied to the data depicted in Figure 6 according to (Gazdag, 1978)

$$\psi\left(x, n\,\Delta z\right) = \frac{1}{2\,\pi}\int \varphi\left(k_x, \omega\right)\alpha\left(k_x, \omega\right) e^{ik_x\,x} dk_x\, d\omega, \tag{6}$$

where spectrum φ is

$$\varphi\left(k_x, \omega\right) = \int \tilde{\psi}_{z(x)}\left(x, \omega\right) e^{ik_x\,x} dx, \tag{7}$$

extrapolation operator α is

$$\alpha\left(k_x, \omega\right) = e^{in\Delta z\,k_z(k_x,\omega)}, \tag{8}$$

and

$$k_z\left(k_x, \omega\right) = \text{sign}\left(\omega\right)\frac{\omega}{c/2}\sqrt{1-\left(\frac{c\,k_x}{2\,\omega}\right)^2}, \tag{9}$$

for $\left(c\,k_x/2/\omega\right)^2 < 1$, and $c/2$ is half the basalt velocity. Note, for $\left(c\,k_x/2/\omega\right)^2 > 1$, $k_z = \Re\left\{k_z\right\} + i\,\left|\Im\left\{k_z\right\}\right|$ *.

The result of ZOM is given in Figure 7. Here, the data of Figure 6 is given in depth for comparison (Figure 7a where $c = 14,000$ cm / μs was used to map $t/2 \rightarrow z$). The ZOM image (Figure 7a) shows good focusing of diffractions events, in particular the diffraction between 4500 and 6500 cm on the input (Figure 7a), and reflection events are generally much more coherent. Noise above the elevation profile (solid line) is evident due to poor constructive interference of primary energy in the nearsurface.

MIGRATE DATA

Though we expect ZOM to return a poor image — especially in the subsurface, it does act a s a good guide for prestack depth imaging (PSDM) as we have now a fair idea of

*Please see the CREWES seismic imaging toolbox and function `gaz_zero_mig`.

where energy should focus. Because georadar data are equivalent to a one-trace common shot gather, we base our georadar PSDM on seismic shot-record migration (Ferguson and Margrave, 2005, for example). The general organization of our georadar PSDM is as follows:

1. Loop over traces.
2. PSDM each trace at $c = 14,000$ cm / μ s.
3. Stack each PSDM in a surface-consistent manner.

For practical implementation, we require that PSDM is run in parallel where we make maximum use of the computational cores available. Our system *Gilgamesh* consists of 19 nodes with 8 cores each. Our strategy, then, is to divide up the total number of traces evenly between nodes and cores. Local to one core, PSDM is applied to each assigned trace in series, with the results stacked into the output array and written to disk. When computation stops, a clean up routine collects and stacks the output from each core into the final image.

Our PSDM is implemented using a set of script files `mssh_psdm`, `run_psdm_radar`, and `psdm_radar` and `gaz_mig` from the CREWES Matlab Toolbox. Rather than use Matlab, however, and have to cope with the parallel implementation of Matlab, we chose instead to modify the Matlab routines slightly to run in Octave. Octave is a free Matlab-like system that we have installed on all 19 *Gilgamesh* nodes.

Implementation begins with a parallel script written in `Pearl` that is run out of a directory that is unique to each line (for line 23, the directory is called LINE23). In each line directory reside the georadar data and imaging code. Pearl script `mssh_psdm` is executed with a pointer to input file `run_psdm_radar`. Input file `run_psdm_radar` provides path names to the line directory and the executable`psdm_radar` plus symbolic pointers to the arguments. The range of traces to be issued to each core within each node is determined by `mssh_psdm` (the `start` and `stop` trace numbers) so that each core processes approximately the same number of traces. `mssh_psdm` then logs on to the selected range of nodes, registers the Octave and disk pathnames, and issues the `psdm_radar` command parametrized with numerical values for `start` and `stop`.

A loop over traces is then initiated by `psdm_radar` to do the actual PSDM and core-local stacking. On each core, `psdm_radar` loads input data and model data, and builds a source model with the source in the middle. Here, we use a unit impulse at the grid level that corresponds to $t = 0$. Beginning with the first (`start`) trace assigned to a given core core, single traces are extracted from the input gather, placed in a `NULL` array corresponding to the acquisition distance from the source location, transformed $(x, t) \Rightarrow (k_x, f)$, band limited to the user-specified range of $f_{min} \leq f \leq f_{max}$, and the source and data spectra, velocity model, Δx, and Δz are passed to `gaz_mig`. `gaz_mig` iterates in depth and applies the imaging condition. Following each psdm in the loop, the results are *stacked* into the output space according to the (x, z) location of the source. With the completion of the core loop, the output stack is written to the line directory.

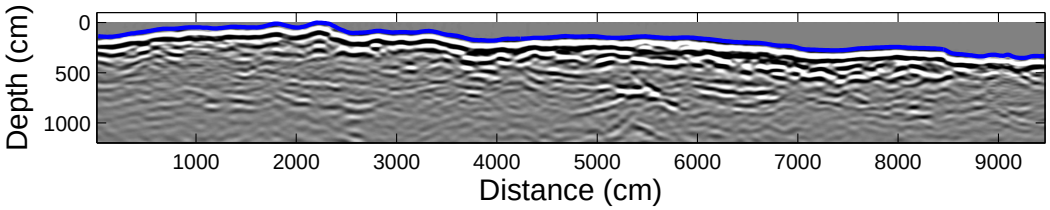

FIG. 8. Stack of all shot record migrations. The elevation profile is overlain as a solid line.

Parameter	Value
Node 1	7
Node N	10
Cores / node	8
# of traces	671
# of psdm traces	1024
# of depths	312
# of stacked traces / core	1695

Table 5. Parallel Octave input parameters.

Following completion of all PSDM's, `stack` loads the stacked data from each core, and does a global stack. Table 5 summarizes the main input parameters. Here, Node 1 and Node N refer to the numbered nodes on Gilgamesh, so nodes 7 / 19 through 10 /19 are used for computation. There are 8 cores per node, and the total number of traces is 621. Because `gaz_mig` is FFT based, the input traces are padded to the nearest power of 2 (1024). The output depth image has 312 grid levels, and each core returns a stacked image that is 1695 traces wide.

For LINE23, the resulting image is given in Figure 8. Apparent immediately is the improved image at the topography level indicated by the solid line. Compared to ZOM (Figure 7b), PSDM has the correct impulse response in the near surface, and constructive interference is much stronger. Deeper down, significant reduction in noise is apparent, and reflections are now more distinct.

Zoom images of ZOM and PSDM are provided in Figures 9a and b respectively. PSDM is clearly superior in the near surface where reflection events are much cleaner and more coherent. Deeper down at 600cm and between 5000 and 6000 cm, the reflection event is much better focused on the PSDM image, and overall, the PSDM image is much cleaner.

CONCLUSIONS

We find that application of leading-edge seismic processing and imaging practice to georadar enhances significantly the final image. In particular, we find that nonstationary deconvolution whitens the spectrum and draws out deeper reflection energy than conventional spiking deconvolution. We find also that prestack depth migration, implemented as single trace shot migration, significantly improves upon the combination of terrain correction followed by zero offset migration.

We implement our georadar imaging algorithm in parallel on our multi-core, multi-node computer cluster, and we use Octave as the central processing language with Linux and Pearl used to effect parallelism. We find that this combination is relatively easy to use, and it is very cost effective in that it uses only freely available software.

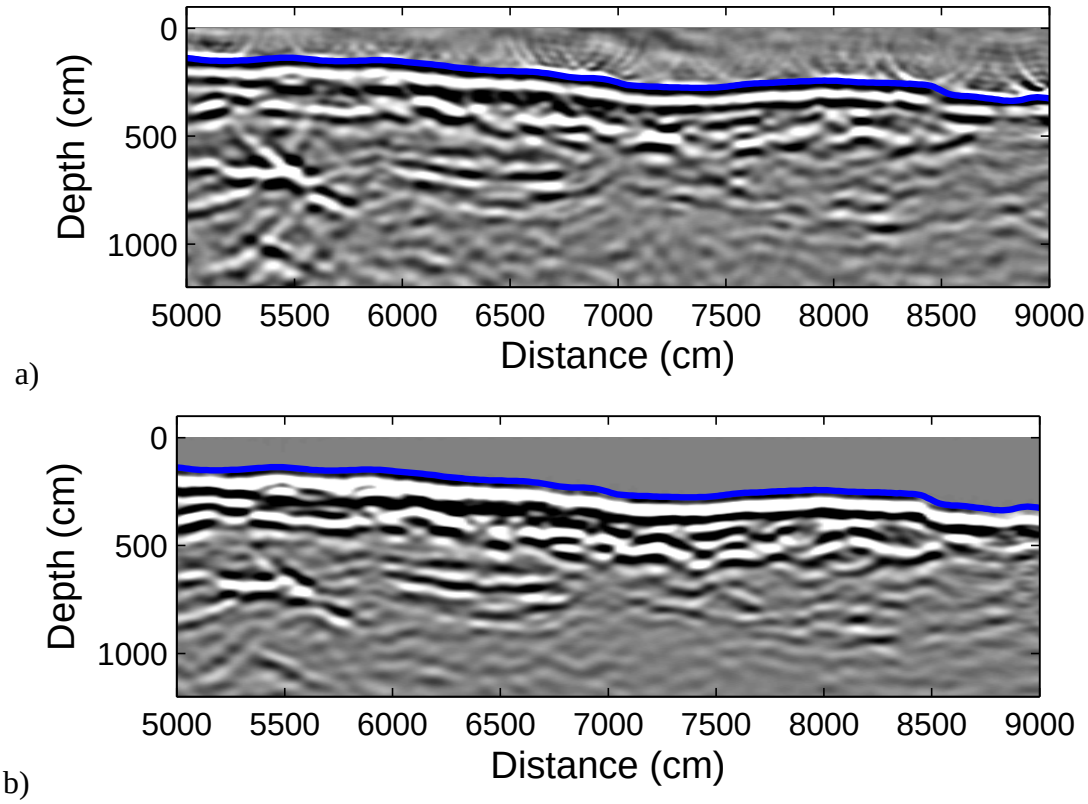

FIG. 9. Migration comparison of 5000-9000 cm. a) Zero offset migration. b) Stacked shot record migration. The shot record migration is less noisy, and energy is more coherent. The elevation profile is overlain as a solid line.

ACKNOWLEDGEMENTS

The authors thank the staff and sponsors of CREWES for their generous support of this research. Further, the authors wish to thank Dr. James D. Irving, School of Engineering, University of Guelph for his advice on acquisition, as well as for the use of his `ekko2mat` georadar to Matlab converter. We also wish to thank Kevin W. Hall of CREWES for his design of the PSDM parallelism.

REFERENCES

Ferguson, R. J. and G. F. Margrave, 2005, Planned seismic imaging using explicit one-way operators: Geophysics, **70**, S101–S109.

Finlay, P. I., N. S. Parry, S. A. Proskin, and R. J. Mickle, 2008, An overview of ice profiling using ground penetrating radar (GPR): SAGEEP Proceedings, 461–470.

Gazdag, J., 1978, Wave equation migration with the phase-shift method: Geophysics, **43**, 1342–1351.

Grasmueck, M., R. W., and H. Horstmeyer, 2005, Full-resolution 3d GPR imaging: Geophysics, **70**, K12–K19.

Jol, H. M., 2009, Ground penetrating radar: Elsevier.

Margrave, G. F., P. C. Gibson, J. P. Grossman, D. C. Henley, V. Iliescu, and M. Lamoureax, 2005, The Gabor transform, pseudodifferential operators and seismic deconvolution: Integrated computer-aided engineering, **12**, 43–55.

Robinson, E. A. and S. Treitel, 1980, Geophysical signal analysis: Prentice-Hall, Inc.

Rowel, C., A. Pidlisecky, and R. J. Ferguson, 2010, Characterization of lava tubes using ground penetrating radar at Craters of the Moon National Monument, Idaho, USA: CREWES Research Reoprt, **22**.

Sen, M. K., P. L. Stoffa, and R. K. Seifoullaev, 2003, Numerical and field investigations of GPR: Towards an airborne GPR: Subsurface Sensing Technologies and Applications, **1**, 41–60.

Slob, E., M. Sato, and G. Olhoeft, 2010, Surface and borehole ground-penetrating-radar developments: Geophysics, **75**, 75A103–75A120.